A Modeling Study of the Effect of the Andes on the Summertime Circulation of Tropical South America

RICHARD KLEEMAN

Bureau of Meteorology Research Centre, Melbourne, Victoria, Australia

(Manuscript received 12 December 1988, in final form 25 May 1989)

ABSTRACT

A simple linear two level model of the atmosphere is developed which has a reasonable representation of the external and tropically important baroclinic modes. By blocking the lower layer of the model with a meridional wall, the interaction between diabatic forcing centered in the Amazon basin and the Andes is studied. This forcing can be considered a source of Rossby waves that scatter from the above partial barrier. The scattering process is examined analytically by making the long-wave approximation, with the conclusion that transmission of external Rossby waves, reflection of baroclinic Kelvin waves, and the creation of topographic jets are likely to be important.

Numerical solutions without the long-wave approximation are then considered and the effects of the above scattering process are examined. The upper level circulation is shown to be qualitatively similar to that obtained without a barrier. The low-level circulation west of the barrier is weak in the winds and consists of a positive geopotential response centered at approximately 30°S. To the east, the circulation near the barrier shows similarity to models of the Somali jet. The model produces quite strong trade winds and places a low-pressure center in approximately the position where one is actually observed.

1. Introduction

The South American tropical region is characterized meteorologically by two important features. First, it is a strong source of diabatic heating which is caused by deep convection over the Amazon basin. Second, it is bounded on the west by the Andes, a very steep and high mountain range that is more or less meridionally oriented. Intuitively one would expect that these two features would be the major influences on the large-scale circulation in this region. It is the intention of this paper to explore this hypothesis. We shall confine our attention to the southern summer as this is the time of strongest convection in the Amazon and also happens to be the period for which observational studies are more complete.

The South American tropical circulation has been studied by a number of observational meteorologists (e.g., see Kreuels et al. 1975; Schwerdtfeger 1975). These studies have been hampered by a lack of station data in certain areas (the western Amazon region is particularly sparse). In view of this it is not surprising that more recent satellite observations (see Virji 1981) have revealed new features in the circulation. The conventional and satellite-derived circulation patterns for the southern summer are depicted in Fig. 1.

The upper level circulation is dominated by an anticyclone over the Bolivian Altiplano and a trough to the east of this. The major difference between the conventional and satellite circulations is the presence in the latter of an extensive zone of easterly winds to the north of the anticyclone. According to Virji, winds in this region may exceed 25 m s^{-1} on certain days.

The low level circulations are broadly similar with an ill-defined area of low pressure being centered at about 25°S and 60°W. The major difference is that the satellite winds show a strong north and northwesterly flow along the eastern side of the Andes. The winds in this region may on certain days be as much as 25 m s^{-1}. This suggests that there may be a low-level jet in this area. This phenomenon is well known to exist off the east coast of Africa in the Somalia region where it is generally thought to be a response to the remote forcing of the Indian monsoon [see Anderson (1978) for an excellent review of this phenomenon]. It should be stressed that the low level observational study of Virji was based on a limited dataset (about 1 week) and should be regarded as preliminary.

Modeling studies of the South American circulation have been undertaken by a number of authors. These authors have been primarily concerned with the upper level circulation and have neglected orographic effects on the implicit assumption that these only affect the low level circulation. Silva Dias et al. (1983) considered a single baroclinic mode linear model with time varying latent heat forcing centered at about 10°S. Such a

Corresponding author address: Dr. Richard Kleeman, Bureau of Meteorology Research Centre, G.P.O. Box 1289K, Melbourne, Victoria, Australia 3001.

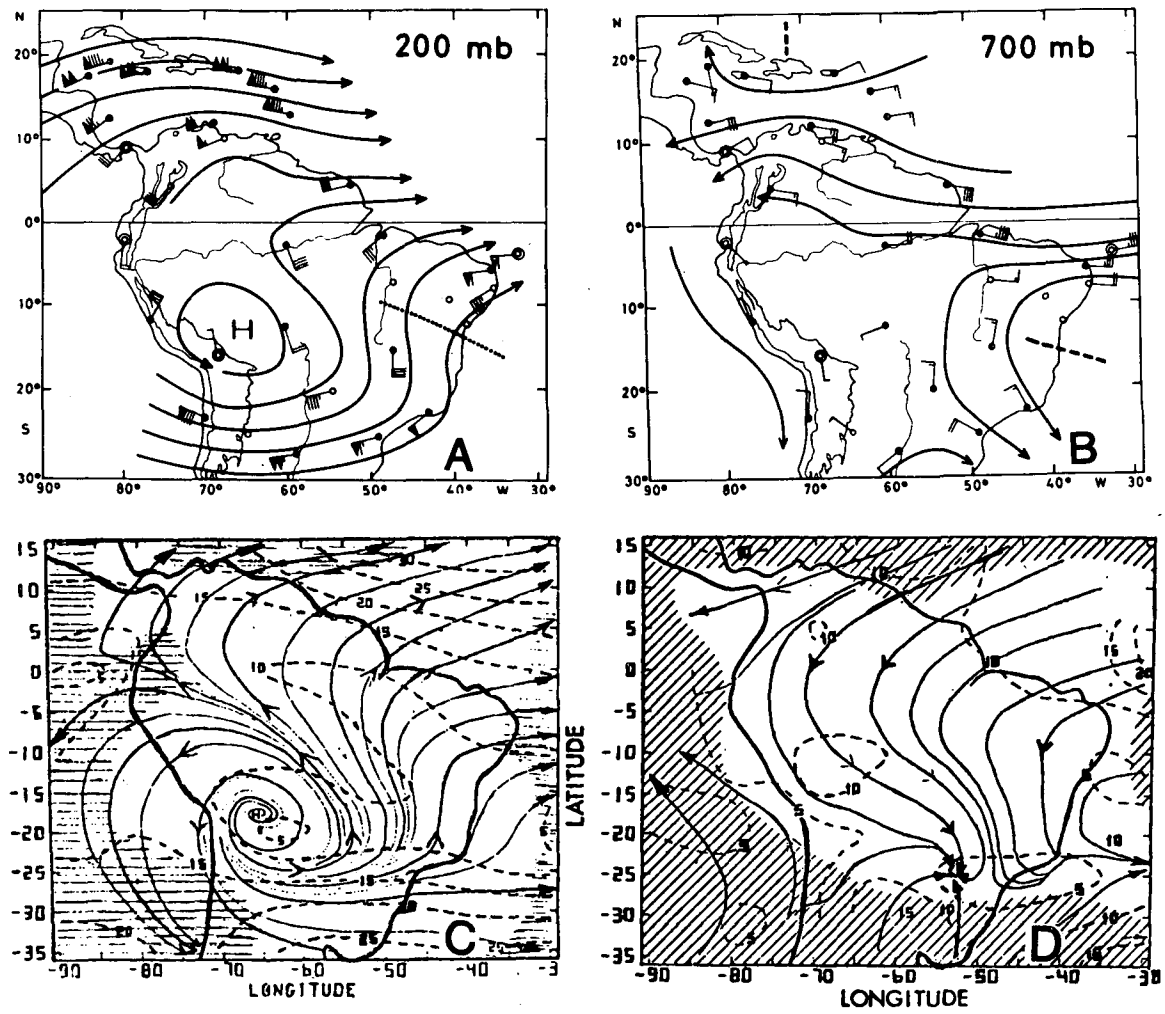

FIG. 1. The upper and lower level circulations of South America during the southern summer. The conventional circulations (a) and (b) are after Kreuels et al. (1975), while the satellite derived circulations (c) and (d) are from Virji (1981). Circulation (c) is based on NESS cloud winds for January and February over three years. Circulation (d) is based on McIDAS cloud winds for six days at the beginning of February 1975.

model is able to simulate the upper level summer circulation quite well: the Altiplano anticyclone in their model is essentially due to the equatorial Rossby wave response to the imposed forcing. This study was extended by DeMaria (1985) to include many vertical modes with the conclusion that the horizontal response is not greatly changed (naturally the vertical response can be significantly different). Buchmann et al. (1986) considered a two level primitive equation model that was forced equally at the 250 mb and 750 mb levels by a time varying latent heating. Again the response was not markedly different to that obtained by Silva Dias et al. Finally the effect of diurnally varying forcing (of importance in the Amazon basin) has been explored with some success by Silva Dias et al. (1987) using a similar model to that discussed initially.

The present study is intended to extend the results of the above authors by including the effect of the Andes. This is achieved by constructing a linear, two pressure level model of the atmosphere whose vertical mode structure consists of an external barotropic mode together with the usual baroclinic mode. The Andes will be simulated by the inclusion of a meridional wall in the lower layer. Such an inclusion of orography has been advocated by Egger (1972a), (1972b), and (1974) in the case in which the mountains are very steep and narrow, a situation certainly pertaining to the Andean range.

A number of authors (Anderson 1976; Sashegyi and Geisler 1987) have studied simple models with complete boundary walls. The major result of such studies is that incident long-wave Rossby modes reflect strongly as short-wave Rossby modes which form strong western boundary jets. Such behavior is put forward as an explanation of the Somali jet in East Africa. As far as this author is aware, the only simple study of a partial wall

was completed recently by McPhaden and Gill (1987). They considered the scattering of a Kelvin wave by such a wall and used the long-wave approximation to construct analytical solutions.

As has been noted by many authors, when the shallow water equations are forced with low frequency diabatic heating the primary response to the west is in the form of long-wave Rossby waves. For the purposes of the present study then, we can regard the Andes as scattering baroclinic long-wave Rossby waves into various reflected and transmitted waves (some may be evanescent and some propagating). As a first step towards understanding this complex process, we shall extend McPhaden and Gill's work (hereafter MG) to the scattering of Rossby waves. The analytical results obtained will be for the long-wave approximation to the model outlined above and will hence ignore reflected short-wave Rossby modes which are undoubtedly important in the formation of western boundary jets. To include such effects one must use the full model for which analytical solutions in closed form appear impossible to obtain. For this reason and for reasons of clarity in examining circulation implications of the partial barrier, the remainder of the paper will consist of numerical model results.

The paper is organized as follows. The models to be used will be derived in section 2. Analytical solutions with the long-wave approximation will be derived and discussed in section 3, and the numerical results from the full model with realistic time varying forcing will be presented in section 4. Section 5 contains an overall discussion of the results.

2. The model equations

Although the models to be discussed in later sections will be two level models we shall construct here an n pressure level model as this will allow for possible future extensions of the current work and because the general model is of some interest in its own right. The vertical deployment of variables in the model are as indicated in Fig. 2.

The momentum equations in pressure coordinates for an equatorial beta plane are

$$\frac{du_i}{dt} - \beta y v_i = -\frac{\partial \Phi_i}{\partial x} \tag{2.1}$$

$$\frac{dv_i}{dt} + \beta y u_i = -\frac{\partial \Phi_i}{\partial y}, \tag{2.2}$$

where i is odd. The hydrostatic equations in the same coordinates are

$$\Phi_{2i+1} - \Phi_{2i-1} = -\overline{\Delta p}_{2i}/\rho_{2i}, \tag{2.3}$$

where $\overline{\Delta p}_{2i} \equiv (\Delta p_{i+1} + \Delta p_i)/2$. This may be modified by use of the ideal gas law to

$$\begin{aligned}\Phi_{2i+1} - \Phi_{2i-1} &= -\frac{RT_{2i}\overline{\Delta p}_{2i}}{p_{2i}} \\ &= -\frac{R\overline{\Delta p}_{2i}}{p_{2i}}\left(\frac{p_{2i}}{1000}\right)^{2/7}\theta_{2i} \\ &\equiv -\Gamma_{2i}\theta_{2i}.\end{aligned} \tag{2.4}$$

The temperature equation is

$$\frac{d\theta_{2i}}{dt} = \left(\frac{1000}{p_{2i}}\right)^{2/7} Q_{2i}, \tag{2.5}$$

where Q_{2i} is the diabatic heating rate (expressed in K s^{-1}). The continuity equation reads

$$\frac{\omega_{2i} - \omega_{2i-2}}{\Delta p_i} = -\nabla \cdot \mathbf{u}_{2i-1}. \tag{2.6}$$

Assuming that there is no perturbation at the top of the atmosphere ($p = 0$), then we have $\omega_0 = 0$, which implies that

$$\omega_{2i} = -\sum_{j=1}^{i} \Delta p_j \nabla \cdot \mathbf{u}_{2j-1} \quad i \leqslant n. \tag{2.7}$$

The system of equations is closed by deriving an equation for ω_{2n}

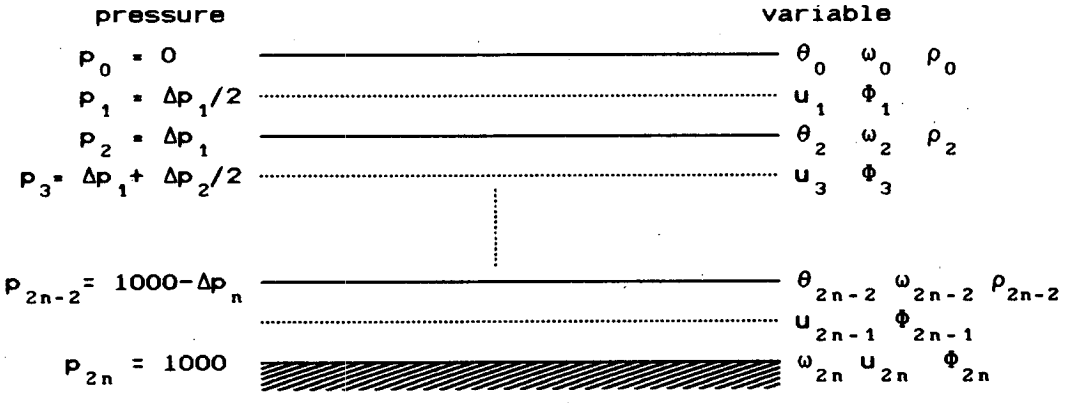

FIG. 2. The vertical deployment of physical variables in the model.

$$\omega_{2n} \equiv \left.\frac{dp}{dt}\right|_{1000\text{ mb}} \approx \left(\frac{\partial p}{\partial t}\right)_z + \mathbf{u}_s \cdot \nabla p_s + w_s \frac{\partial p}{\partial z}, \quad (2.8)$$

where the subscript s denotes a surface value.

Now we have the following:

$$\left(\frac{\partial p}{\partial t}\right)_z = \left(\frac{\partial p}{\partial t}\right)_p - \frac{\partial p}{\partial z}\left(\frac{\partial z}{\partial t}\right)_p$$

$$= \rho_s g\left(\frac{\partial z}{\partial t}\right)_p \approx \rho_{2n}\frac{\partial \Phi_{2n}}{\partial t}.$$

Likewise it follows easily that

$$\nabla_z p_s = \nabla_p p_s + \rho_s g \nabla_p z \approx \rho_{2n}\nabla_p \Phi_{2n}.$$

Hence with the use of $w_s = 0$, we obtain

$$\omega_{2n} \approx \rho_{2n}\left[\mathbf{u}_{2n}\cdot\nabla\Phi_{2n} + \frac{\partial \Phi_{2n}}{\partial t}\right]. \quad (2.9)$$

The right-hand side of this equation is significantly nonzero, contrary to the assumptions of many models found in the literature. A condition very similar to (2.9) is used in the linearized continuously stratified theory to include the Lamb or external mode (see Gill 1982, p185). The assumption that $\omega_{2n} = 0$ is equivalent to the assumption that the barotropic mode is nondivergent (i.e., it has an infinite shallow water speed). To close the system we assume that the variations in Φ and $\mathbf{u}$ at 1000 mb are proportional to those at the next lowest level [the $(2n-1)$th level]. Thus we have

$$\omega_{2n} = \rho_{2n}\sigma\left(\gamma\mathbf{u}_{2n-1}\cdot\nabla\Phi_{2n-1} + \frac{\partial\Phi_{2n-1}}{\partial t}\right), \quad (2.10)$$

where we shall assume that $\sigma \approx 1.0$ and $\gamma \approx 0.7$.

In the linear model the advection term is dropped and so we have the approximate relation

$$\omega_{2n} \approx \rho_{2n}\sigma\frac{\partial\Phi_{2n-1}}{\partial t}, \quad (2.11)$$

and hence

$$\omega_{2n-2} = \rho_{2n}\sigma\frac{\partial\Phi_{2n-1}}{\partial t} + \Delta p_n \nabla\cdot\mathbf{u}_{2n-1}. \quad (2.12)$$

For the linear model, Eq. (2.5) is linearized about a state of rest and constant vertical potential temperature gradient. When this is combined with Eqs. (2.4), (2.7), and (2.12) we obtain

$$(\Phi_{2i-1} - \Phi_{2i+1})_t + \sum_{j=1}^{i} G_n(2i,j)\nabla\cdot\mathbf{u}_{2j-1} = F_{2i}Q_{2i}$$

$$\{[1+\delta(n)]\Phi_{2n-1} - \Phi_{2n-3}\}_t$$

$$+ G_n(2n-2,n)\nabla\cdot\mathbf{u}_{2n-1} = -F_{2n-2}Q_{2n-2}, \quad (2.13)$$

where $i \leqslant n-1$ and

$$G_n(2i,j) = -\frac{\overline{\partial\theta}}{\partial p}\Delta p_j \Gamma_{2i}; \quad F_{2i} = R\frac{\overline{\Delta p}_{2i}}{p_{2i}}$$

$$\delta(n) = -\sigma\rho_{2n}\frac{\overline{\partial\theta}}{\partial p}\Gamma_{2n-2}. \quad (2.14)$$

We fix $\rho_{2n} = 1.2$ kg m^{-3} and $\dfrac{\overline{\partial\theta}}{\partial p} = 6.25 \times 10^{-4}$ °C Pa^{-1}.

The linearized versions of Eqs. (2.1) and (2.2) together with Eqs. (2.13) and (2.14) constitute the linear model. We note that a further advantage of choosing $\sigma \neq 0$, apart from realism, is the fact that we have n (rather than $n-1$) tendency equations for Φ which makes numerical integration of the model simpler.

The vertical mode structure and the appropriate energy equation for the two-level model are derived in appendix A. The vertical mode form of the variables may be written as

$$q_a = \gamma_1 q_1 + \gamma_2 q_3$$

$$q_b = \gamma_3 q_1 - \gamma_4 q_3, \quad (2.15)$$

where the γ_i are the transformation coefficients from the level to vertical mode variables and the subscripts a and b refer to the particular vertical mode under consideration. For realistic values of the physical parameters and $\Delta p_1 = \Delta p_2$ we obtain $c_a = 295.3$ m s^{-1} and $c_b = 59.3$ m s^{-1} for the vertical mode shallow water speeds. These are reasonable values for the external mode of the atmosphere and the baroclinic mode, which receives most of the diabatic forcing. We also have

$$(\gamma_1)^2 + (\gamma_2)^2 = 1 = (\gamma_3)^2 + (\gamma_4)^2, \quad (2.16)$$

with $\gamma_1 = \gamma_4 = 0.74$, and $\gamma_2 = \gamma_3 = 0.67$. The justification for the names barotropic and baroclinic for the two vertical modes is now apparent.

3. The scattering of Rossby waves in the long-wave approximation

In this section we obtain analytical solutions for the scattering process. The long-wave approximation is required to obtain solutions, and, as was mentioned in the Introduction, this implies that western boundary currents are only treated implicitly. We nondimensionalize the equations for both the baroclinic and barotropic modes by choosing velocity scale $V = c_b$ (the baroclinic shallow water speed) and length scale $L = (c_b/\beta)^{1/2}$. The long-wave approximation is made by dropping the meridional velocity tendencies and for both modes the replacement diagnostic equation is

$$yU + \frac{\partial\Phi}{\partial y} = 0. \quad (3.1)$$

As has been observed by many authors (see MG for example), the horizontal modes are separable with the y dependence being given by

$$\Phi_K{}^i(y) = D_0(\alpha_i y); \quad U_K{}^i = \alpha_i{}^2 D_0(\alpha_i y); \quad V_K{}^i = 0$$
$$\Phi^i_{Rm}(y) = (m+2)D_m(\alpha_i y) + D_{m+2}(\alpha_i y)$$
$$U^i_{Rm}(y) = [-(m+2)D_m(\alpha_i y) + D_{m+2}(\alpha_i y)]\alpha_i{}^2$$
$$V^i_{Rm}(y) = D_{m+1}(\alpha_i y), \tag{3.2}$$

where $m \geq 0$, the D_n are the parabolic cylinder functions, the subscripts K and R refer to Kelvin and Rossby modes, respectively, and the i superscript denotes the vertical mode with

$$\alpha_i = (c_b/c_i)^{1/2}.$$

We place the barrier at $x = 0$ and require that the following conditions be met across it at the two model levels:

$$u_1(0^+) = u_1(0^-)$$
$$\Phi_1(0^+) = \Phi_1(0^-)$$
$$u_3(0^-) = 0$$
$$\int_{-\infty}^{\infty} u_3(0^+)dy = 0. \tag{3.3}$$

The notation 0^+ and 0^- denotes the limit at x approaches 0 from the east and west, respectively. The final condition in (3.3) is the long-wave western boundary condition (see Cane and Sarachik 1977). As has been discussed in MG, this condition is required rather than $u_3(0^+) = 0$ since only Kelvin waves are available to propagate energy towards the east. The short-wave Rossby waves, which constitute the boundary currents in the full equations, are confined to a narrow meridional strip and they have small meridionally integrated zonal mass flux—hence the boundary condition.

Consider now a Rossby wave incident on the barrier. As was pointed out in MG, the dynamical variables at the barrier are separable with respect to y and t. The meridional dependence to the east of the barrier can be written for m even as

$$U^b(y) = R^b D_0(y) + \Delta^m(D_{m+2}(y) - (m+2)D_m(y))$$
$$U^a(y) = \alpha^2 R^a D_0(\alpha y)$$
$$\Phi^b(y) = R^b D_0(y) + \Delta^m(D_{m+2}(y) + (m+2)D_m(y))$$
$$\Phi^a(y) = R^a D_0(\alpha y), \tag{3.4}$$

where the incident Rossby amplitude is Δ^m while R^a and R^b represent the reflected Kelvin wave amplitudes for the two vertical modes. We have also defined $\alpha \equiv \alpha_a$.

To the west of the barrier the geopotential fields must have similar functional forms in order to satisfy the matching conditions (3.3). Thus we can write

$$\underline{\Phi}^b(y) = A^b + B^b D_0(y) + C^b D_0(\alpha y) + E^b D_m(y) + F^b D_{m+2}(y)$$

and similarly for $\underline{\Phi}^a$. The nonzero constant term A^b is possible here because Eq. (3.1) ensures its nonappearance in the equation for $\underline{U}^b$. Hence the matching conditions (3.3) do not force it to be zero as would happen for any other functional form not appearing in (3.4). Now Eq. (3.1) together with the parabolic cylinder function identity (B.2) imply

$$y\underline{U}^b(y) = yB^b D_0(y) + \alpha^2 yC^b D_0(\alpha y) + yE^b D_m(y) + yF^b D_{m+2}(y) - 2^{1/2}[mE^b D_{m-1}(y) + (m+2)F^b D_{m+1}(y)]. \tag{3.5}$$

The second line of this may be rewritten as

$$-2y\{(m+2)D_m(y)F^b + [E^b - (m+2)F^b]\sum_{i=0}^{m/2-1}[(-1)^i m(m-2)\cdots(m-2i)D_{m-2i-2}(y)]\}, \tag{3.6}$$

with the second term of this expression vanishing for $m = 0$. Consider now three cases. For $m = 0$ we may, without loss of generality, let $E^b = (m+2)F^b$. For $m = 2$ the same condition may be established by use of the second and third conditions in (3.3). For $m > 2$, the condition again holds because the coefficient of $D_{m-2}(y)$, which occurs in $\underline{U}^a$ and $\underline{U}^b$ [cf. (3.6)], is zero when the conditions in (3.3) involving u_i are used. Thus we may write, using (3.5) and (3.6):

$$\underline{\Phi}^b = A^b + B^b D_0(y) + C^b D_0(\alpha y) + F^b[(m+2)D_m(y) + D_{m+2}(y)]$$
$$\underline{U}^b = B^b D_0(y) + \alpha^2 C^b D_0(\alpha y) + F^b[-(m+2)D_m(y) + D_{m+2}(y)], \tag{3.7}$$

with similar equations holding for $\underline{U}^a$ and $\underline{\Phi}^a$. The third condition from (3.3) now implies that

$$F^a = (\gamma_4/\gamma_3)F^b;$$
$$C^a = (\gamma_4/\gamma_3)C^b;$$
$$B^a = (\gamma_4/\gamma_3)B^b. \tag{3.8}$$

The second condition from (3.2) implies that

$$\gamma_2 A^b + \gamma_1 A^a = 0$$
$$\gamma_2 B^b + \gamma_1 B^a = \gamma_2 R^b$$
$$\gamma_2 C^b + \gamma_1 C^a = \gamma_1 R^a$$
$$\gamma_2 F^b + \gamma_1 F^a = \gamma_2 \Delta^m. \quad (3.9)$$

Note that F^b and F^a are now determined:

$$F^a = \gamma_2\gamma_4\Delta^m/G; \quad F^b = \gamma_2\gamma_3\Delta^m/G \quad (3.10)$$

where $G = \gamma_2\gamma_3 + \gamma_1\gamma_4$. The first condition from (3.3) is redundant because of our imposition of (3.1). The long-wave western boundary condition gives us the equation

$$\gamma_3\alpha R^a = \gamma_4(R^b - \Delta^m Z_m), \quad (3.11)$$

where

$$Z_m = \begin{cases} (m-1)(m-3)\cdots 1 & m > 0 \\ 1 & m = 0. \end{cases}$$

The form of the transmitted amplitudes is restricted by the requirement that they represent a sum of Rossby modes. This restriction applies to both vertical modes and can be written as

$$\int_{-\infty}^{\infty} (\underline{\Phi}^b + \underline{U}^b) D_0(y)\,dy = 0 \quad (3.12)$$

$$\int_{-\infty}^{\infty} (\underline{\Phi}^a + \alpha^{-2}\underline{U}^a) D_0(\alpha y)\,dy = 0. \quad (3.13)$$

Equation (3.12) leads to the equation

$$A^b + 2^{1/2}B^b + (1+\alpha^2)^{1/2}C^b = 0, \quad (3.14)$$

while Eq. (3.13) gives

$$\alpha A^a + (1+\alpha^2)^{1/2}B^a + 2^{1/2}\alpha C^a + \frac{\alpha^2 - 1}{(1+\alpha^2)^{1/2}}\left[\frac{1-\alpha^2}{1+\alpha^2}\right]^{m/2} Z_m F^a = 0, \quad (3.15)$$

where we are using a result derived in appendix B. We now have sufficient equations to determine a solution.

Equations (3.9), (3.8), and (3.11) can be combined to obtain

$$C^b = \gamma_1\gamma_3 R^a/G = \gamma_1\gamma_4(R^b - Z_m\Delta^m)/(\alpha G)$$
$$B^b = \gamma_2\gamma_3 R^b/G, \quad (3.16)$$

and this allows us to rewrite (3.14) as

$$A^b = -[2^{1/2}\gamma_2\gamma_3 + (1+\alpha^{-2})^{1/2}\gamma_1\gamma_4]R^b/G + (1+\alpha^{-2})^{1/2}\gamma_1\gamma_4 Z_m\Delta^m/G. \quad (3.17)$$

A similar equation can be obtained by using (3.16) and (3.8) in Eq. (3.15). When this equation is combined with (3.17) we obtain

$$R^b = Z_m\Delta^m \frac{(1+\alpha^2)^{1/2} + 2^{1/2}[(\gamma_1\gamma_4)/(\gamma_2\gamma_3)] + (1-\alpha^2)/(1+\alpha^2)^{1/2} \times [(1-\alpha^2)/(1+\alpha^2)]^{m/2}}{2(1+\alpha^2)^{1/2} + 2^{1/2}[(\gamma_1\gamma_4)/(\gamma_2\gamma_3) + \alpha(\gamma_2\gamma_3)/(\gamma_1\gamma_4)]} \quad (3.18)$$

For m odd the solution is considerably simpler since in this case it is antisymmetric about the equator which prevents a Kelvin wave reflection. We therefore have

$$U^b(y) = \Delta^m[D_{m+2}(y) - (m+2)D_m(y)]$$
$$U^a(y) = 0$$
$$\Phi^b(y) = \Delta^m[D_{m+2}(y) + (m+2)D_m(y)]$$
$$\Phi^a(y) = 0. \quad (3.19)$$

To the west of the barrier we must have

$$\underline{\Phi}^b = E^b D_m(y) + F^b D_{m+2}(y)$$
$$y\underline{U}^b = y[E^b D_m + F^b D_{m+2}] - 2^{1/2}[mD_{m-1}E^b + (m+2)F^b D_{m+1}].$$

If y is set equal to zero in this equation it easily follows using (A.1) that $E^b = (m+2)F^b$ as in the even case. Hence

$$\underline{\Phi}^b = F^b[(m+2)D_m + D_{m+2}]$$
$$\underline{U}^b = F^b[-(m+2)D_m + D_{m+2}] \quad (3.20)$$

and similarly for the other vertical mode. Note that this implies that the meridional structure of the transmitted baroclinic Rossby wave is identical with the incident wave. The solution for amplitudes in this case is trivial. The second and third conditions from (3.3) combine to give (3.10), which is the complete solution. The other conditions are satisfied automatically and the transmitted wave is always a linear combination of Rossby modes if it is antisymmetric.

To examine the effect of the barrier in a more transparent manner, we calculate the energy fluxes through the barrier. The total flux across the barrier may be written as (see appendix A):

$$\text{FLUX} = \frac{2}{G^2}\left\{[(\gamma_4)^2 r + (\gamma_3)^2(1-r)]\int_{-\infty}^{\infty} \Phi^a u^a\,dy + [(\gamma_2)^2 r + (\gamma_1)^2(1-r)]\int_{-\infty}^{\infty} \Phi^b u^b\,dy\right\} \quad (3.21)$$

where $r = \Delta p_1/1000$.

Each vertical mode may be further separated into an incident Rossby flux, a reflected Kelvin flux, and a transmitted Rossby flux. In the case of incident Rossby waves there is, as in the case of a full barrier (see Clarke

1983), a substantial loss of long-wave energy to short-wave Rossby modes, which are not modeled and physically represent western boundary jets.

The dependence of the fluxes on the parameters σ [see Eq. (2.10)] and r may be seen in Figs. 3 and 4. The incident flux is chosen to be the baroclinic vertical mode and the first symmetric and antisymmetric horizontal modes. For reference the baroclinic and barotropic shallow-water speeds together with γ_1 and γ_3 are also plotted.

As can be seen from Fig. 3, the fluxes are not very sensitive to the choice of σ despite the fact that the barotropic shallow water speed undergoes large variations. This provides reassurance that the parameterization used in section 2 is a robust one.

The sensitivity to r (Fig. 4) is more substantial, with the transmitted baroclinic Rossby flux being particularly affected. One should not interpret these results as indicating the sensitivity of fluxes to variations in the height of the barrier in the real atmosphere, however,

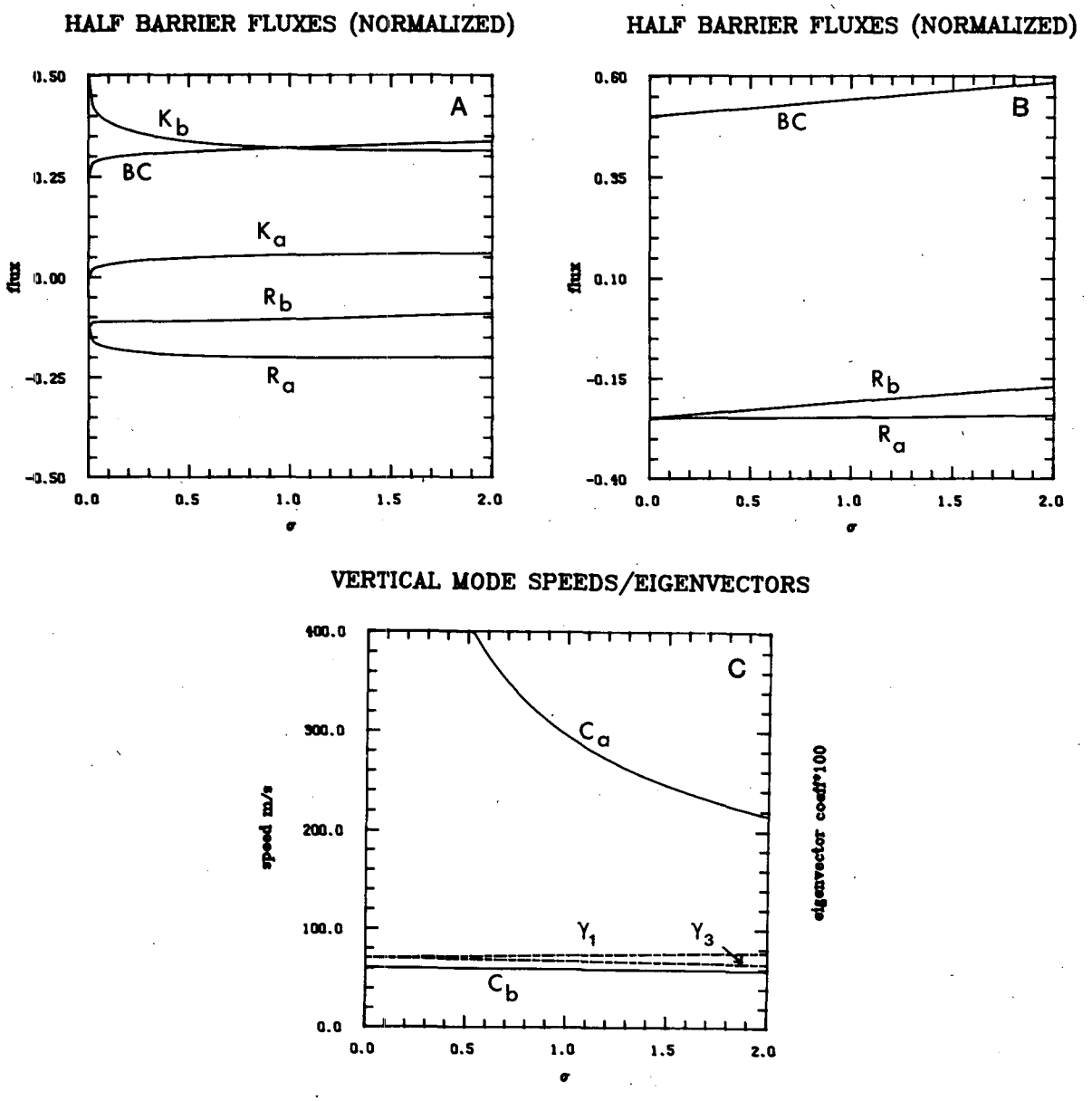

FIG. 3. The dependence of scattered fluxes from an incident baroclinic Rossby mode on the parameter σ. (a) For the case where the incident mode is the lowest order symmetric mode, (b) for the case of the lowest order asymmetric mode. Here R_a and R_b refer respectively to transmitted barotropic and baroclinic Rossby fluxes; K_a and K_b to reflected barotropic and baroclinic Kelvin fluxes; and BC is the residual flux assumed to go into boundary currents. (c) The barotropic and baroclinic shallow water speeds (C_a and C_b), and also these modes' projections onto the upper level (γ_1 and γ_3).

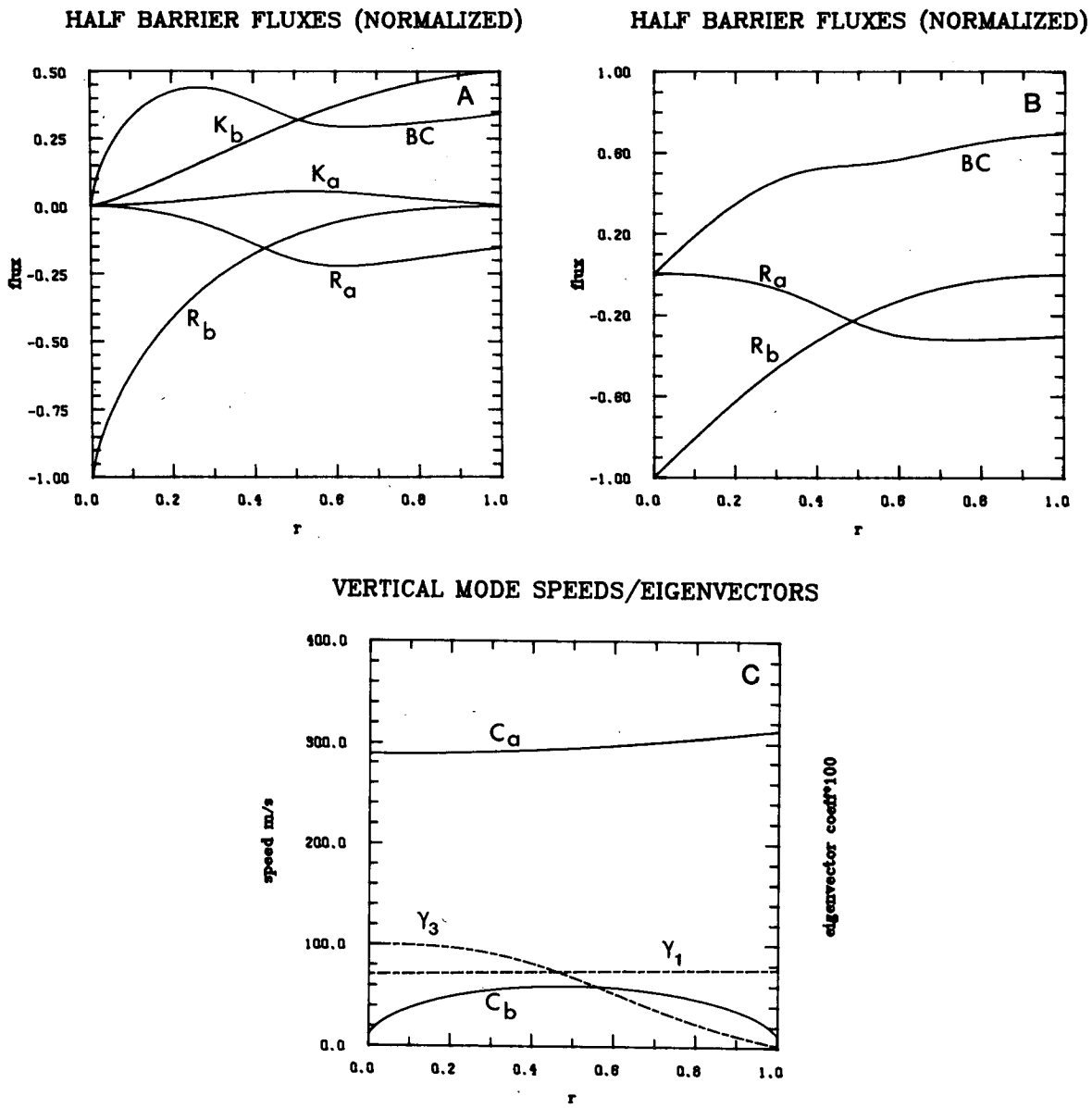

FIG. 4. The same as Fig. 3 but illustrating sensitivity to the parameter r which measures the partitioning of pressure levels.

since the variation of r also strongly affects the vertical mode structure of the model (see Fig. 4c). Thus as r approaches zero (ostensibly an infinitely high barrier) the baroclinic mode becomes more and more concentrated in the upper layer and becomes less and less like the predominant baroclinic mode of the real tropical atmosphere. Similar comments apply as r approaches 1. A better study of the effect of the height variation would be to solve the many level (many vertical mode) problem with varying levels of blocking. We do not attempt such a study here.

The case of an incident symmetric baroclinic Rossby mode of varying meridional mode structure can be seen in Fig. 5. Perhaps the most significant comment to be made here is that as n becomes large, the symmetric fluxes approach the antisymmetric ones, which are independent of n. The $n = 0$ case shows an approximately equal three-way split between transmitted Rossby modes, reflected Kelvin modes and the short-wave Rossby sink. The n = odd and n large and even case, shows an approximately equal two-way split between transmitted Rossby modes and the short-wave sink. The implication of this result is that diabatic forcing which is a "long" distance from the equator (such as that of the Indian monsoon) will strongly generate antisymmetric and higher order Rossby modes and

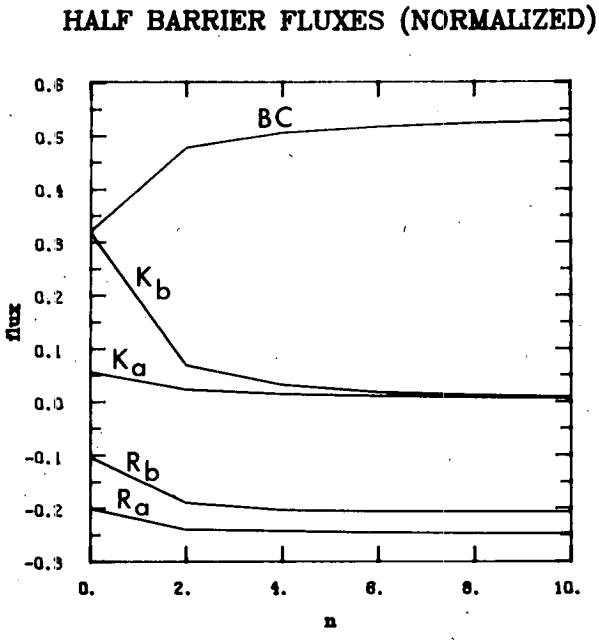

FIG. 5. The sensitivity of fluxes to the type of incident symmetric baroclinic Rossby mode. Here $n = 0$ is the lowest order symmetric mode, $n = 2$ the next lowest.

hence generate a stronger short-wave Rossby response (western boundary jet) at the barrier than diabatic forcing closer to the equator (such as the Amazonian forcing). Since this latter forcing may be expected to strongly generate $n = 0$ Rossby modes one would expect from the above results, to observe a substantial baroclinic Kelvin mode reflection from the barrier in this case.

An interesting aspect of the above results is the conversion of baroclinic to barotropic Rossby waves. For large variations in the parameters, this amounts to around 20% of the incident baroclinic Rossby flux. Given that the Bolivian upper-level anticyclone is an indication that the Amazonian diabatic forcing is strongly generating Rossby modes, this would appear to be a potentially important source of barotropic energy in the tropics.

4. Numerical results from a linear model

In this section we drop the long-wave approximation since we are concerned with the form of possible western boundary jets. We shall use the simple two-level linear model derived in section 2 since the success of Silva Dias et al. (1983) in accounting for many of the observed upper level circulation features with a simple single baroclinic mode model suggests that this approach is fruitful. As noted in the Introduction, numerical methods must be used when the long-wave approximation is dropped.

Also following Silva Dias et al., we shall consider the case of time-varying forcing. Convective bursts with time scales of around two to three days shall be the focus of our attention. Consideration of diurnally varying forcing, which is clearly important, shall be deferred to a later publication.

The model used for numerical experimentation was the two level linearized version of Eqs. (2.1), (2.2), and (2.13). The horizontal structure of the forcing was chosen to be

$$Q(x, y) = \begin{cases} Q_0 \exp[-(y + D)^2/2D^2] \sin[\pi(x + S)/ \\ \qquad 7 \times 10^6], \quad 0 < x < L \\ 0, \quad \text{otherwise} \end{cases} \tag{4.1}$$

with $S = 3.0 \times 10^6$, $D = 10^6$ m, and $L = 4 \times 10^6$ m, which are reasonable values for representing the southern summer diabatic forcing in the Amazon region.

The time dependence was chosen to be identical with that used by Silva Dias et al. (1983), namely

$$Q(x, y, t) = Q(x, y) \frac{\alpha}{2} \alpha^3 t^2 e^{-\alpha t}, \tag{4.2}$$

with $\alpha^{-1} = 6$ h. The parameter Q_0 in Eq. (4.1) was adjusted so that the time averaged heating rate over three days had a value of 6°C per day. The partial barrier was imposed by blocking the lower layer as follows:

$$u_3(0, y) = 0. \tag{4.3}$$

The time dependent equations were integrated from a state of rest using an explicit leapfrog scheme with a time filter to suppress the computational mode. An Arakawa C-grid with spacing of 140 km was used in the horizontal. This enabled the boundary condition for the meridional walls to be easily specified. A meridional wall blocking both layers was inserted at $x = 17\,200$ km and $x = -18\,800$ km. This form of boundary condition was preferred over cyclic conditions as the effects to the west of the half barrier could then be clearly separated from those to the east (where the forcing was located). Zonal blocking walls at $y = \pm 15\,000$ km were inserted to complete the integration domain. The equations were integrated for three days by which time the forcing was close to zero.

As has been demonstrated by Anderson (1976), the lack of dissipation in models of western boundary jets with steady forcing implies that the width and strength of the jets indefinitely decrease and intensify respectively. This does not pose a problem for this study since the forcing used diminished rapidly after an initial maximum and the time integration extended over only 3 days. The zonal grid resolution used was more than adequate for resolving the jet over this period (and hence preventing numerical instability). Naturally one should not take too seriously the values of wind speeds obtained, as dissipative processes evidently play a significant role in determining such strengths.

The results of the integration at times 0.75 days, 1.5 days, and 3 days may be seen in Fig. 6. For reference the difference between the upper level circulation with and without the barrier also is depicted.[1]

As may be observed, the upper level circulation results are qualitatively not very different from those obtained without a barrier by Silva Dias et al. (1983). This situation tends to confirm the implicit assumption made in earlier modeling that the barrier does not greatly affect the upper levels of the atmosphere. The Altiplano anticyclone is situated in approximately the correct position with respect to the barrier after about a day. The difference fields (barrier minus nonbarrier) are fairly complex. The major features are as follows:

1) The westerlies to the east of the barrier are enhanced by around 25%. This appears to be due to the reflection from the barrier of *baroclinic* Kelvin waves.

2) The geopotential field to the west of the barrier is strengthened in such a way that the anticyclone is stretched towards the west. Associated with this effect, the northerly winds to the west of the anticyclone are weakened. These changes appear to be due to westward propagating *barotropic* Rossby waves.

3) There is some evidence that the barrier causes the trough to the east of the anticyclone to intensify.

4) The easterly flow over the barrier in the equatorial region is weakened. This would appear to be due to the attenuation of the baroclinic Rossby waves by the barrier.

The low-level circulation can be divided into an eastern and a western circulation, with the barrier dividing the two regions. In the eastern region the solution at 0.75 and 1.5 days shows a number of qualitative similarities with the circulation of Fig. 1. There is (particularly at 1.5 days) an equatorially trapped region of easterlies extending eastward from the source of heating. At 1.5 days these trade winds are quite strong as indeed they are in Fig. 1. This strength can be traced to the baroclinic Kelvin wave reflection from the barrier. The northeasterly winds seen over the Amazon basin in Fig. 1 are evident at 0.75 days but by 1.5 days have disappeared. The solution at 3 days is presumably dissimilar to Fig. 1 because by this stage dissipative processes not modeled here have become important. This degradation in agreement was observed in all the model runs undertaken.

The situation near the barrier is (from about 1 day on) qualitatively similar to the solutions obtained by Anderson (1976) when modeling the Somali jet with a one-layer model. A cross-equatorial jet adjacent to the barrier[2] separates from the barrier somewhat to the south of the equator and heads toward the center of the forcing; another jet in the opposite direction, exists adjacent to the barrier and further poleward of the first. It is somewhat difficult to compare the model results near the barrier with the observations in Fig. 1. This is due to the fact that from about 10° to 20°S the Andean mountain range is actually oriented northwest–southeast. To overcome this problem we shall modify the half-barrier appropriately. The results from this model run are considered below.

The solution for the western region consists entirely of a positive geopotential response with regions of high geopotential propagating and elongating southwest and northwest of the barrier (the former region being the stronger). The winds associated with these circulations are much weaker than those seen in the eastern region; however, the geopotential values are a sizable fraction (around 40%) of those seen to the east. The circulation overall shows strong qualitative similarities with that seen in the eastern Pacific. There are, however, strong reasons for doubting that the Amazonian heating is the main influence on this circulation. First, the winds involved are too small by a factor of 5 to 10. Second, this circulation is observed even when the heating is located to the north of the barrier (the southern winter); model results (see below) with northern forcing do not generate the same kind of circulation. There remains the possibility, however, that this heating is influential in the variability of the circulation.

The rest of this section shall consist of further model results concerning the eastern low-level circulation. The first model to be considered is essentially the above model with the half-barrier modified to more accurately reflect the Andes in the Peruvian–Bolivian region. From 8°S to 18°S the barrier runs at 45°, while at either end of this segment it extends meridionally to the edge of the integration domain. In addition, horizontal diffusion is included in the momentum equations as this has been suggested by Anderson (1976) as the best method of modeling the dissipative processes acting on the boundary jets. The value chosen for the diffusion coefficient was 2×10^5 m^2 s^{-1}, which was close to Anderson's value. In order to deal with the above boundary conditions, the finite differencing grid was altered to that illustrated in Fig. 7. The geopotential gradient terms in the velocity tendency equations and the divergence terms in the geopotential tendency equations were finite differenced as follows:

$$(\Phi_{ij} - \Phi_{i-1j})/\Delta x \quad \text{(tendency equation for } u_{ij})$$

$$(\Phi_{i-1j+1} - \Phi_{i-1j} + \Phi_{ij} - \Phi_{ij-1})/2\Delta y$$

(tendency equation for v_{ij})

$$(u_{i+1j} - u_{ij})/\Delta x + (v_{ij+1} - v_{ij} + v_{i+1j} - v_{i+1j-1})/2\Delta y$$

(tendency equation for Φ_{ij}).

[1] It may be of some value to readers to compare these figures with Fig. 4 from Silva Dias et al. (1983) where a meridional mode decomposition is carried out.

[2] The closest meridional wind grid point to the barrier is omitted in Fig. 6 for clarity. The maximum velocities are around 20 m s^{-1}; that is about twice those of the next grid point.

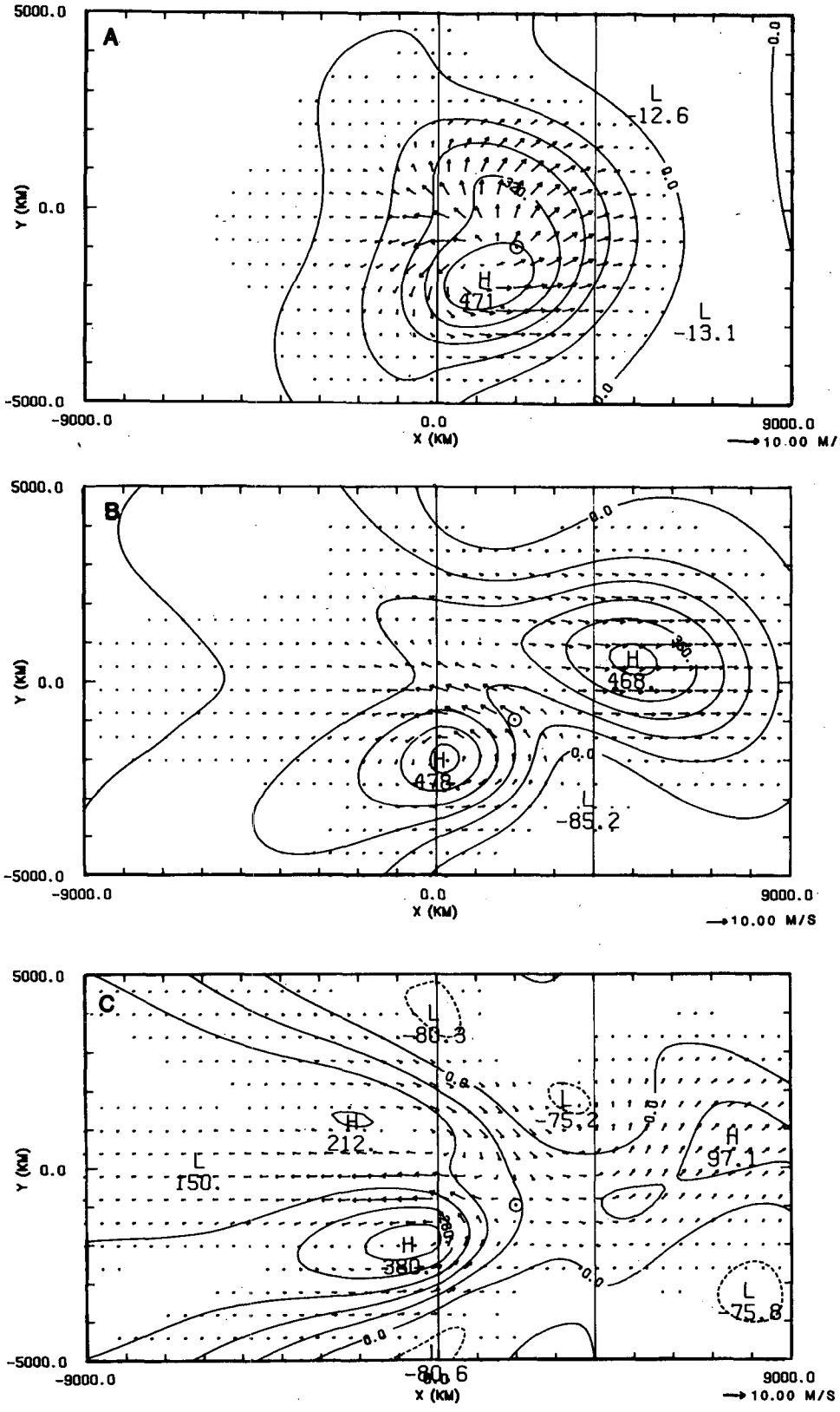

FIG. 6. The model results at times 0.75 days, 1.5 days, and 3 days. Here (a) through (c) are the upper level results; (d) through (f) are the barrier minus no barrier results for the upper level; (g) through (i) are the western lower level results; and (j) through (l) are the eastern lower level results. The character ⊙ is at the latitude of peak forcing and at the longitude which is geographically the center of the forcing. The vertical lines included represent the eastern and western extremities of the diabatic forcing.

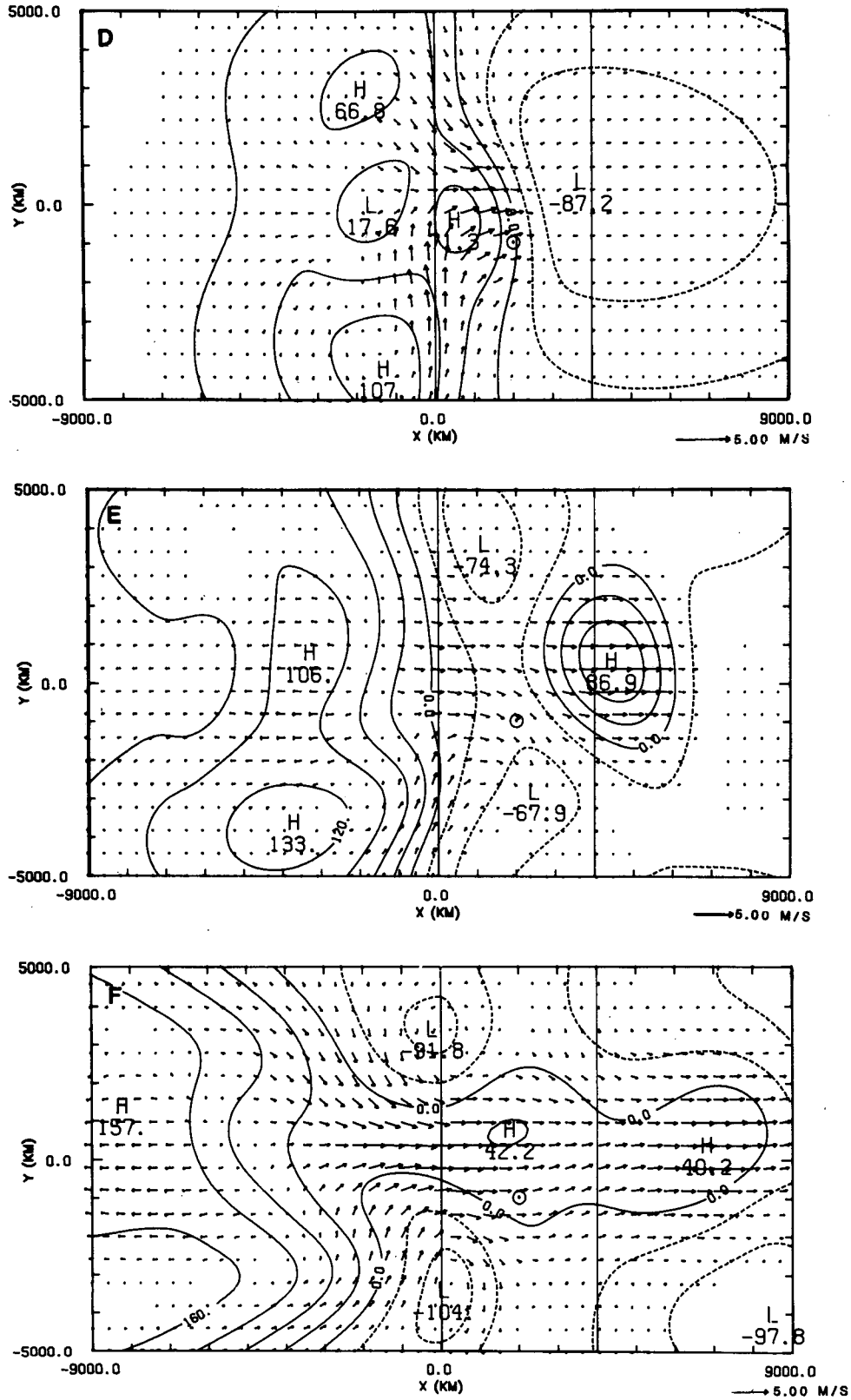

FIG. 6. (*Continued*)

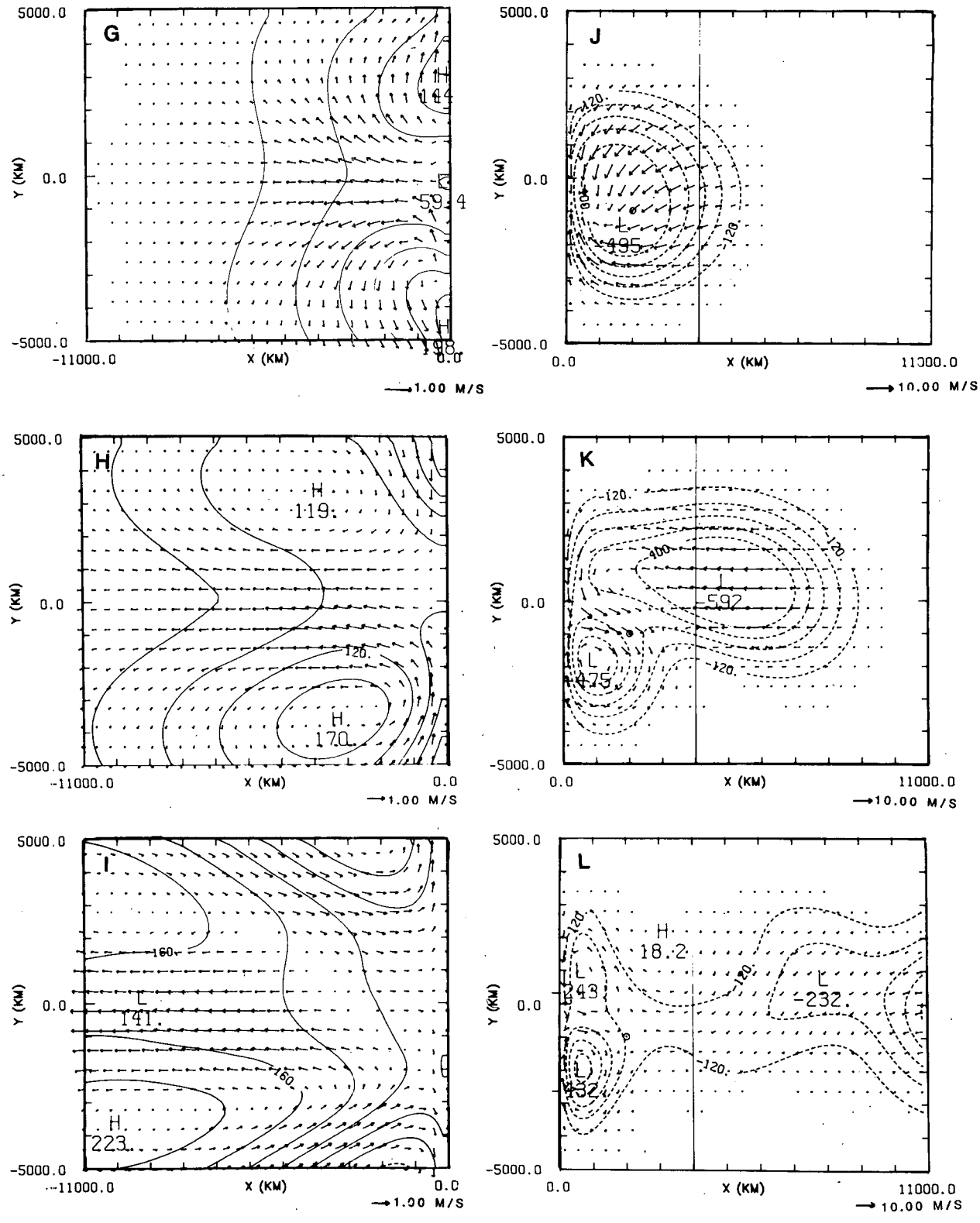

FIG. 6. (*Continued*)

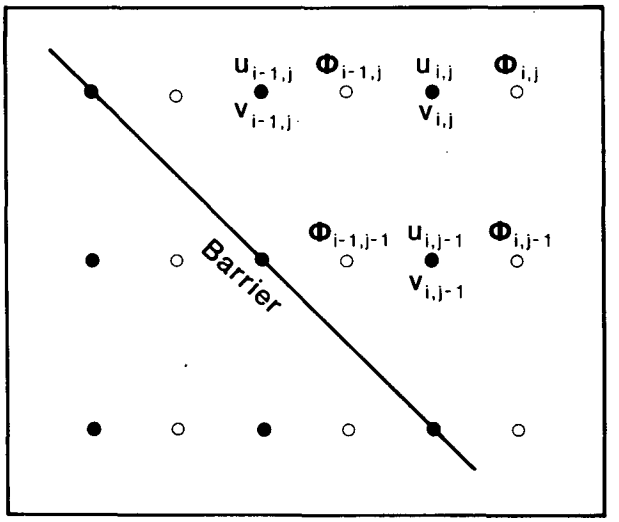

FIG. 7. The horizontal staggering of variables for the model with a more realistic simulation of the Andes (see text). Note that the zonal and meridional grid spacings are equal, meaning that the diagonal barrier is oriented exactly northwest–southeast.

This scheme enabled a straightforward treatment of equations near the diagonal barrier. The barrier itself was imposed by setting both u_3 and v_3 to zero. The southern and northern boundaries (now located at $y = \pm 9000$ km) were specified by setting all fields to zero. The diffusion was increased smoothly from $y = \pm 7000$ km to the boundaries so that at the boundaries the coefficient was 2×10^7. This was done to prevent numerical noise generation in this region.

The circulation at 1.5 days may be seen in Fig. 8. Comparison with Fig. 1 shows a number of agreements. These are: the trade winds in the Atlantic are strong; the flow near the Andes is qualitatively correct in its direction and approximately correct in its magnitude in comparison with the trades; there is a low-level cyclone in approximately the correct position with respect to the Andes; and, finally, there is a northerly flow over southeastern Brazil.

The discrepancies are as follows: The flow along the angled part of the Andes seen in Fig. 1 actually detaches from the barrier in the model[3] and the model jet appears to be too far north; there is an extensive northeasterly flow over northern Brazil not simulated by the model at 1.5 days (it is, however, seen earlier in the integration); and lastly the simulated cyclone is probably somewhat north of where observations place it. One reason for the latter discrepancy is that continental thermal effects probably contribute significantly to the observed low pressure center as well. Another possibility is that recent outgoing longwave radiation observations indicate that the heating may be farther south than that chosen here (the author wishes to thank an anonymous referee for this latter explanation).

The strength and width of boundary jets is dependent on the nature and strength of dissipative processes in operation. In order to examine this in the present model, the horizontal diffusion coefficient was reduced by a factor of 10. The principal effect was to narrow and strengthen the flows near the boundary at the equator and at 20°S. The velocities in these regions increased by about a factor of 2. The northwesterly flow seen at 1.5 days strengthened by about 50% while the Atlantic easterlies increased only slightly.

Nonlinear effects may be important to the circulation details. In order to examine this possibility the following procedure was adopted: the low level equations were modified by inserting the appropriate advection terms; the tendency equation for the low-level geopotential involves the upper-level divergence which was specified to be that of the linear model. Although this procedure is somewhat artificial it should give some rough understanding of the role of the advection terms.

The circulation at 1.5 days may be seen in Fig. 9. Compared to the linear model, the winds in the northwesterly and westerly flow are considerably strengthened while the northerly flow adjacent to the Andes and further north is not changed. This effect was also seen by Anderson (1976) and in view of Fig. 1 increases agreement with observations. The Atlantic easterlies are also strengthened as are the geopotential minima (including the cyclone at 20°S).

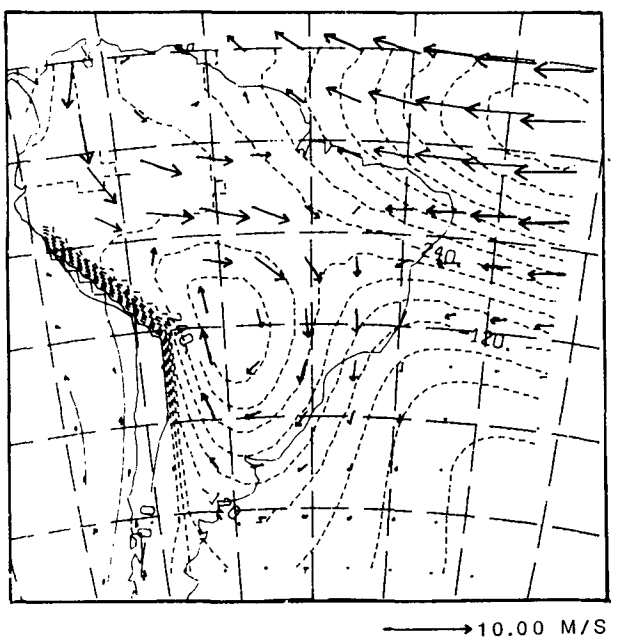

FIG. 8. The eastern low-level circulation at 1.5 days. The barrier is located on the eastern side of the sharp gradient of geopotential and its northern section is located where the contours vanish.

[3] Figure 3b from the paper by Virji (1982) gives the circulation for a single day and clearly shows evidence of a westerly flow, i.e., detachment from the barrier. This flow is still more southerly than that of the model.

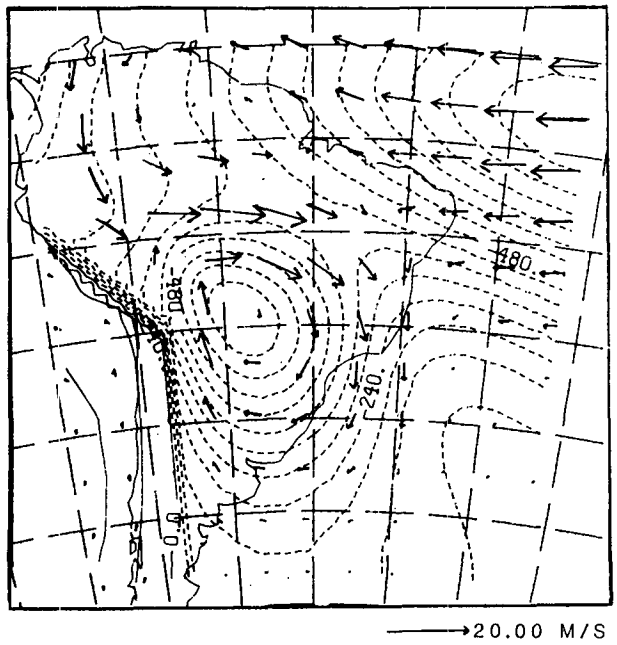

FIG. 9. The same as Fig. 8 but with nonlinear advection terms included in the lower layer equations (see the text).

Some further observational evidence for the low-level circulation modeled above and its association with convective bursts can be seen in the FGGE analyses of early- to mid-February 1979. The analyses for 11–13 February at 850 mb and 200 mb may be seen in Fig. 10. The upper level circulations for the first two days were used by Silva Dias et al. (1983) as support for their modeling study of time dependent convective activity. In the low-level analyses, a circulation pattern similar in some respects to that of Virji (and hence the modeled circulation) can be clearly seen to be developing through the three days in question. In particular, a northwesterly jet can be seen strengthening at approximately 13°S, 63°W which is close to where a similar feature was observed by Virji. In contradistinction to the model results however, the analyses here show only marginal signs of a propagating pulse of low-level easterlies in the equatorial Atlantic.

The Andes do not, as has been modeled here, extend indefinitely to the north and south. In order to see whether this finite length has any bearing on the circulation features discussed above, the barrier was truncated at 10°N and 40°S to more accurately simulate the low-level blocking effect. There was little change observed in the circulation to the east of the barrier (a slight weakening of the trades was evident). To the west of the barrier the low-level positive geopotential effect was more confined to the Southern Hemisphere.

In two final experiments, the position of the forcing was altered. The forcing of Eq. (4.1) peaks close to the barrier consistent with the rainfall estimates of Kreuels et al. Given the doubts expressed previously over the location of this heating, this was modified so that the peak rainfall was located in the middle of the Amazon basin. The x dependence was chosen to be

$$1.07 \sin(\pi x/4 \times 10^6), \qquad (4.4)$$

with the extra factor included so that the horizontally integrated forcing was identical to that used previously. Compared with the previous experiment a number of differences were observed in the low-level circulation at 1.5 days: The northwest and west flow was stronger and extended farther north; the cyclone at 20°S was enhanced and a stronger southerly flow existed between the cyclone and the barrier.

It is also of some interest to examine the consequences of locating the forcing in a position more typical of the southern winter. To examine this situation the above forcing was centered meridionally at approximately 10°N and zonally at the barrier (but extending on both sides). In addition the barrier was truncated at approximately 8°N. This crudely simulates the positioning of diabatic forcing in Central America and northern South America. The circulation was now quite different, and with two exceptions resembled qualitatively the situation pertaining when no barrier was present [see Silva Dias et al. (1983) for the equivalent circulation in the Southern Hemisphere]. The exceptions to this qualitative agreement were as follows: First, a reasonably strong south to southeasterly flow was observed adjacent to the eastern side of the barrier extending from the equator to 10°N. Second, and possibly more interestingly, an intense low at the lower level was seen propagating southward along the western side of the barrier. The propagation speed of this disturbance was approximately 60 m s^{-1}. At the upper level, a weaker low pressure area developed more or less in situ near the barrier. It was located primarily to the west of the barrier (although not exclusively) and at around 40°S. As time progressed it spread slowly towards the southwest. The low-level behavior is strongly reminiscent of a coastal Kelvin wave as discussed in an atmospheric context by Gill (1977) and Anh and Gill (1981). It is hoped to further analyze this interesting feature in a future paper.

A rather curious aspect concerning the presence of the barrier is the energetics. For the inviscid run above, it was found that the domain integrated total energy [defined as the integral of the quantity in square brackets in Eq. (A.7)] asymptoted to a 15% higher value when the barrier was present. The reason for this is probably to be found in the source term of (A.7) which shows that the rate of energy addition depends on the product of the heating and a quantity approximately equal the baroclinic component of the geopotential. Now if this second quantity changes as a result of the barriers presence, as it will because of reflection, the energy added to the system will change even though the heating remains the same. Since there is apparently a strong baroclinic Kelvin wave reflection in this model

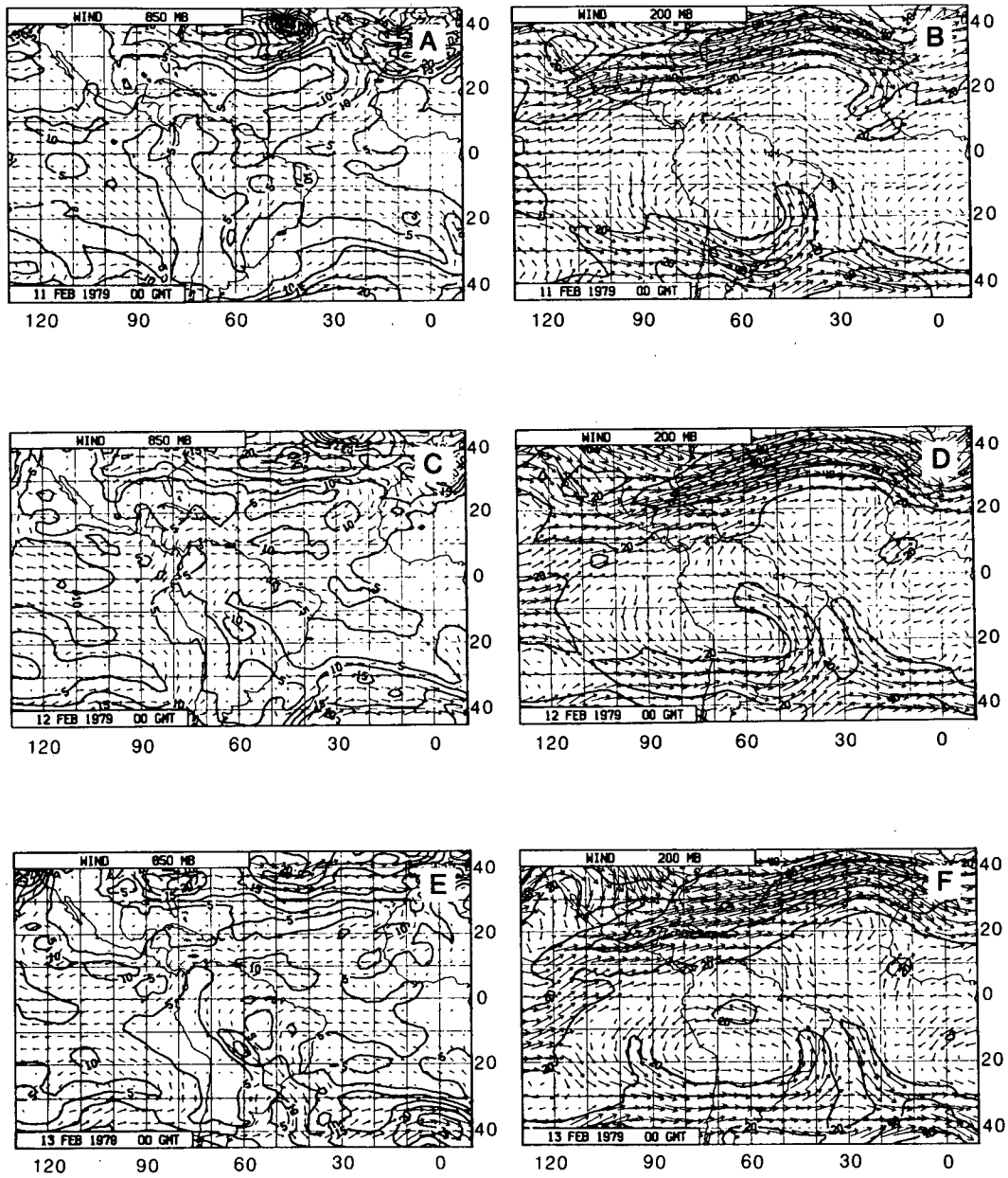

FIG. 10. The FGGE III-B ECMWF analyses of the tropical South American region for 11–13 February 1979. The dates and levels of the analyses are on the diagrams.

the reason for the higher energy observed can be understood.

5. Summary and discussion

A number of simple models have been used to examine the effect on the southern summer South American circulation of the Andes.

The Amazonian region is a strong diabatic heating source and hence in a linear model, can be expected to be a strong source of low-order equatorial baroclinic Rossby modes (the presence of the Bolivian upper level anticyclone supports this suggestion) which propagate towards the west and scatter from the partial barrier provided by the Andes.

This scattering process was examined analytically in section 3 with the use of the long-wave approximation. The conclusion of this study was that three processes may be important: The back reflection of baroclinic Kelvin modes; the conversion of incident baroclinic Rossby modes to barotropic Rossby modes; and the generation of boundary jets adjacent to the barrier as

a result of the back reflection of short-wave Rossby modes.

The implications of this scattering process for the circulation were examined using numerical models in section 4. The qualitative features of the upper-level circulation were similar to those obtained without a barrier, with the Bolivian anticyclone being reproduced in approximately the correct position. Compared to the no barrier case, the westerly winds of the equatorial Atlantic were stronger while the anticyclone was more elongated towards the west. The former effect can be traced to the baroclinic Kelvin mode reflection, while the latter appears to be due to the transmitted barotropic Rossby modes. Evidence of this barotropic response can be seen in the work of Silva Dias and Bonatti (1985) who examined the vertical mode structure of the region. Their Fig. 6 shows some indication of an external mode anticyclone to the west of the Andes. Interestingly this figure indicates that the external mode makes a significant contribution to the easterly flow over the Andes (this occurs to the north of the Bolivian anticyclone). Decomposition of the model results of section 4 into vertical modes shows that this is also the case in the model.

The western low-level circulation obtained was similar to that actually observed although considerably weaker in the winds. Another way of understanding this model response is as follows. The forcing in the Amazon generates downward motion to the west of the barrier. The low level region to the west is isolated from the east and can thus be considered as a single layer responding to the input of mass from above. Such a forcing may be expected (Gill 1980) to generate an anticyclonic response that will be predominantly to the southwest if the forcing is in the Southern Hemisphere (as it mainly is in the model runs above). Evidence for such forcing can be clearly seen in various analyses of the 500 mb vertical velocity (e.g., see Silva Dias et al. 1987; Ardanuy and Krishnamurti 1987) where a strong patch of downward motion can be seen centered just off the coast of northern Chile. Whether the diabatic forcing of the Amazon has any significant effect on the circulation of the far southeastern Pacific remains unclear. As was pointed out previously, the model results here *do not* support the hypothesis that the circulation is *primarily* caused by Amazonian heating since the model winds are far too weak, and also because a similar circulation is observed during the southern winter when the modeled circulation is quite different. The large geopotential changes in this region in the model do, however, suggest some possible influence. To help resolve this question a careful observational study is clearly required.

The modeled eastern low-level circulation has two important features. First, it has strong Atlantic easterlies associated with baroclinic Kelvin modes as discussed above. Second, the response near the barrier is quite similar to that observed in models of the East African jet (modeled as a response to the Indian monsoon diabatic forcing). When more realistic topography is used the circulation obtained shows some agreement with the observational study of Virji. This agreement is further improved by including nonlinear terms in the model. Perhaps the major deficiency of the model is that it places the westward moving stream near the Andes too far to the north. One possible explanation for this may lie in the dissipative process of cumulus momentum mixing. The northerly side of the stream may be more strongly dissipated than the southern side due to both the convection and the upper-level winds being more intense on this side. A further reason may be that the real low pressure center is located more to the south than that observed in the model because of thermal effects, and this position may imply a more southward location for the westward flow as well. Whether there are jets in the western Amazon comparable in strength with that seen off the coast of Somalia remains unclear from this study. Certainly the model results suggest the potential for such a phenomenon but it should be stressed that the strength of jets in the model depend heavily on the level of dissipation. Dissipative processes along the eastern side of the Andes are likely to be stronger than those in the vicinity of Somalia because of the strong convective activity and hence cumulus momentum mixing. It is clear that a more extensive observational study is required to address this issue more sensibly.

Another interesting aspect of this modeling study is that the northeast flow seen in observations over the northeastern sector of the continent is seen only in the first day of the model runs. The model flow at this stage is predominantly baroclinic in this area, while the observational flow is not. The observed upper level flow is southwest only along the north coast of the continent. This suggests there may be a significant barotropic flow in the area, as can be seen in Fig. 6 of Silva Dias and Bonatti. Two possible reasons for this flow are: First, the model may be underestimating the backflux of barotropic Kelvin waves, and second there may be a significant transmitted flux from incident Pacific baroclinic Kelvin waves.

A number of avenues of investigation are suggested by the results of this paper. It is reasonably straightforward to generalize the results of section 3 to a many level model. Such a generalization would be useful in investigating the effect of varying the height of the barrier. The effect on the low-level circulation of strong thermal forcing in the Chaco area of Paraguay and northern Argentina deserves investigation. A full primitive equation model would be useful in confirming the conclusions regarding nonlinearity and the low-level circulation reached in the previous section. The upper-level implications of nonlinearity would also be of some interest. The interesting barrier trapped low-level disturbance seen in the case of southern winter forcing would seem to merit further analysis. Finally,

the consequences of cumulus momentum mixing in the Amazon need to be explored.

Acknowledgments. The author wishes to thank the two anonymous referees for suggesting significant improvements to the manuscript. Useful discussions with Neville Smith and Lance Leslie of BMRC are also acknowledged.

APPENDIX A

Vertical Structure and Energy Equation for the Model

The vertical mode structure is derived for the two-level model. The extension to many levels is straightforward. In matrix form the temperature equation of the linear model is

$$\mathbf{J}\underline{\Phi}_t + \mathbf{G}\nabla\cdot\underline{\mathbf{u}} = \underline{Q} \tag{A.1}$$

where

$$\mathbf{J} = \begin{bmatrix} 1 & -1 \\ -1 & 1+\delta(2) \end{bmatrix}; \quad \underline{Q} = \begin{bmatrix} F_2Q_2 \\ -F_2Q_2 \end{bmatrix};$$

$$\mathbf{G} = \begin{bmatrix} G_2(2,1) & 0 \\ 0 & G_2(2,2) \end{bmatrix}.$$

Now let the vertical mode decomposition be

$$\underline{\Phi}^v = \mathbf{A}\underline{\Phi} \qquad \underline{\mathbf{u}}^v = \mathbf{A}\underline{\mathbf{u}} \quad \text{where} \quad \mathbf{A} = \begin{bmatrix} \gamma_1 & \gamma_2 \\ \gamma_3 & -\gamma_4 \end{bmatrix}. \tag{A.2}$$

It follows that

$$\mathbf{J}\mathbf{A}^{-1}\underline{\Phi}_t^v + \mathbf{G}\mathbf{A}^{-1}\nabla\cdot\underline{\mathbf{u}}^v = \underline{Q}$$

$$\underline{\Phi}_t^v + \mathbf{A}\mathbf{J}^{-1}\mathbf{G}\mathbf{A}^{-1}\nabla\cdot\underline{\mathbf{u}}^v = \mathbf{A}\mathbf{J}^{-1}\underline{Q}. \tag{A.3}$$

Now if Eq. (A.3) is to be a pair of shallow water equations we require that

$$\mathbf{A}\mathbf{J}^{-1}\mathbf{G}\mathbf{A}^{-1} = \begin{bmatrix} c_a^2 & 0 \\ 0 & c_b^2 \end{bmatrix}, \tag{A.4}$$

or in other words, the columns of $\mathbf{A}^{-1}$ are eigenvectors of $\mathbf{J}^{-1}\mathbf{G}$, while the c_a^2 and c_b^2 are proportional to the corresponding eigenvalues. The decomposition into vertical modes now can be solved.

The vertically integrated perturbation energy equation for the continuously stratified problem in isobaric coordinates may be written (see Gill 1982, p 187) as

$$\frac{1}{2}\frac{\partial}{\partial t}\Bigg\{\int_0^{1000}\Bigg[\underbrace{u^2+v^2}_{1,2}+\underbrace{\frac{1}{\Gamma Z}\left(\frac{\partial\Phi}{\partial p}\right)^2}_{3}\Bigg]dp + \underbrace{\rho_0\Phi^2(1000)}_{4}\Bigg\} + \underbrace{\int_0^{1000}\nabla\cdot(\mathbf{u}\Phi)dp}_{5} = -\int_0^{1000}\frac{Q}{\Gamma}\left(\frac{\partial\Phi}{\partial p}\right)dp, \tag{A.5}$$

where Γ is minus the pressure derivative of the background potential temperature, while Z is defined as

$$Z = \frac{R}{p}\left(\frac{p}{1000}\right)^{2/7}.$$

The third and fourth terms on the left-hand side are the perturbation available potential energy while the fifth term is simply the divergence of the horizontal energy flux. The right-hand side of this equation is the diabatic heating source/sink.

We now obtain a vertical finite difference version of this equation for the case $\Delta p_1 = \Delta p_2$ as follows[4]: Take the inner product of the momentum equations with $\underline{u}$ and $\underline{v}$ and Eq. (A.1) with $\frac{1}{G_2(1)}\underline{\Phi}$. Upon adding the result we obtain

$$\frac{1}{2}\frac{\partial}{\partial t}\left[\underline{u}^t\underline{u}+\underline{v}^t\underline{v}+\frac{1}{G_2(1)}\underline{\Phi}^t\mathbf{J}\underline{\Phi}\right]+\nabla\cdot(\underline{\mathbf{u}}^t\underline{\Phi}) = \frac{-Z(500)\Delta p}{G_2(1)}Q(500)(\Phi_3-\Phi_1), \tag{A.6}$$

or in expanded form

$$\frac{1}{2}\frac{\partial}{\partial t}\left[u_1^2+v_1^2+u_3^2+v_3^2+\frac{(\Delta p)^2}{G_2(1)}\frac{(\Phi_3-\Phi_1)^2}{(\Delta p)^2}+\frac{\delta(2)}{G_2(1)}(\Phi_3)^2\right]+\nabla\cdot(\mathbf{u}_1\Phi_1+\mathbf{u}_2\Phi_2) = \frac{-(\Phi_2-\Phi_1)}{\Gamma(500)\Delta p}Q(500), \tag{A.7}$$

when use is made of the expressions given above for $\delta(2)$ and $G_2(1)$ one can clearly see that (A.7) is analogous to (A.5) with the vertical integrals being estimated in an obvious manner. Note that setting $\sigma = 1$ makes the final term in the square brackets in (A.7) a consistent estimate for the analogous term in (A.5).

One can now transform Eq. (A.6) into the vertical mode form obtaining:

$$\frac{1}{2}\frac{\partial}{\partial t}\left[(\underline{u}^v)^t\underline{u}^v+(\underline{v}^v)^t\underline{v}^v+\frac{1}{G_2(1)}(\underline{\Phi}^v)^t\mathbf{K}\underline{\Phi}^v\right] + \nabla\cdot((\underline{\mathbf{u}}^v)^t\underline{\Phi}^v) = \frac{-Z(500)\Delta p}{G_2(1)}(\underline{\Phi}^v)^t\mathbf{A}\mathbf{Q}, \tag{A.8}$$

where we are using the orthogonality of $\mathbf{A}$ (which holds when $\Delta p_1 = \Delta p_2$) and where

$$\mathbf{K} = \mathbf{A}\mathbf{J}\mathbf{A}^{-1} = (\mathbf{A}\mathbf{J}^{-1}\mathbf{A}^{-1})^{-1} = G_2(1)\begin{bmatrix} c_a^{-2} & 0 \\ 0 & c_b^{-2} \end{bmatrix}. \tag{A.9}$$

[4] The generalization is quite straightforward. Note that we use the notation $G_2(1) = G_2(2,1)$.

When the equalitites in (A.9) are applied to the right-hand side of (A.8), it becomes clear that this equation simply expresses the conservation of the sum of the usual shallow-water energies. This conservation law is given by (see Gill 1982):

$$\frac{1}{2}\frac{\partial}{\partial t}\left[u^2+v^2+\frac{1}{c^2}(\Phi)^2\right]+\nabla\cdot(\mathbf{u}\Phi)=\frac{1}{c^2}F\Phi, \tag{A.10}$$

where F is the usual forcing of the third equation.

APPENDIX B

A Parabolic Cylinder Function Identity

The recurrence relation for the functions may be written as

$$D_{m+1}(y)=(2)^{1/2}yD_m(y)-mD_{m-1}(y), \tag{B.1}$$

while the raising and lowering operations may be expressed as

$$\left(\frac{\partial}{\partial y}+y\right)D_m(y)=2^{1/2}mD_{m-1}(y)$$

$$\left(\frac{\partial}{\partial y}-y\right)D_m(y)=-2^{1/2}D_{m+1}(y). \tag{B.2}$$

We now establish the following identity which holds for m even:

$$\int_{-\infty}^{\infty}D_m(y)D_0(\alpha y)dy=Z_m\left[\frac{1-\alpha^2}{1+\alpha^2}\right]^{m/2}\frac{(2\pi)^{1/2}}{(1+\alpha^2)^{1/2}}, \tag{B.3}$$

where Z_m was defined in Eq. (3.11). For $m=0$ the result follows by use of a change of variables in the normalization condition for $D_0(y)$. Now it follows easily from (B.2) that

$$\left(\frac{\partial}{\partial y}-\alpha^2y\right)D_m(\alpha y)=-(2)^{1/2}\alpha D_{m+1}(\alpha y) \tag{B.4}$$

$$\left(\frac{\partial}{\partial y}-\alpha^2y\right)D_m(y)=\frac{1-\alpha^2}{(2)^{1/2}}mD_{m-1}(y)-\frac{1+\alpha^2}{(2)^{1/2}}D_{m+1}(y). \tag{B.5}$$

Remembering that the $\{D_l(\alpha y)\}$ form a complete orthogonal set in L_2, we can take the L_2 inner product of both sides of (B.5) with $D_0(\alpha y)$ and observe that the left-hand side of the resulting equation vanishes when (B.4) is used. We therefore obtain for all m

$$\int_{-\infty}^{\infty}D_{m+1}(y)D_0(\alpha y)dy=m\left[\frac{1-\alpha^2}{1+\alpha^2}\right]\int_{-\infty}^{\infty}D_{m-1}(y)D_0(\alpha y)dy. \tag{B.6}$$

The result (B.3) now holds trivially.

REFERENCES

Anderson, D. L. T., 1976: The low-level jet as a western boundary current. *Mon. Wea. Rev.*, **104,** 907–921.

——, 1978: Orographically controlled cross-equatorial flow. *Orographic Effects in Planetary Flows,* R. Hide, Ed., GARP Publ. Ser. No. 23, 317–355.

Anh, N. N., and A. E. Gill, 1981: Generation of coastal lows by synoptic-scale waves. *Quart. J. Roy. Meteor. Soc.*, **107,** 521–530.

Ardanuy, P. E., and T. N. Krishnamurti, Divergent circulations inferred from Nimbus-7 ERB: Application to the 1982–1983 ENSO Event. *J. Meteor. Soc. Japan,* **65,** 353–370.

Buchmann, J., P. L. Silva Dias and A. D. Moura, 1986: Transient convection over the Amazon Bolivia region and the dynamics of droughts over north-east Brazil. *Arch. Meteor. Geophys. Bioklim. Ser. A.*, **34,** 367–384.

Cane, M. A., and E. S. Sarachik, 1977: Forced baroclinic ocean motions. II. The linear equatorial bounded case. *J. Mar. Res.*, **35,** 395–432.

Clarke, A. J., 1983: The reflection of equatorial waves from oceanic boundaries. *J. Phys. Oceanogr.*, **13,** 1193–1207.

DeMaria, M., 1985: Linear response of a stratified tropical atmosphere to convective forcing. *J. Atmos. Sci.*, **42,** 1944–1959.

Egger, J., 1972a: Incorporation of steep mountains into numerical forcasting models. *Tellus,* **24,** 324–335.

——, 1972b: Numerical experiments on the cyclogenesis in the Gulf of Genoa. *Beitr. Phys. Atmos.*, **45,** 320–346.

——, 1974: Numerical experiments on lee cyclogenesis. *Mon. Wea. Rev.*, **102,** 847–860.

Gill, A. E., 1977: Coastally-trapped waves in the atmosphere. *Quart. J. Roy. Meteor. Soc.*, **103,** 431–440.

——, 1980: Some simple solutions for heat-induced tropical circulation. *Quart. J. Roy. Meteor. Soc.*, **106,** 447–462.

——, 1982: *Atmosphere-Ocean Dynamics.* Academic Press, 662 pp.

Kreuels, R., K. Fraedrich and E. Ruprecht, 1975: An aerological climatology of South America. *Meteor. Rundsch.*, **28,** 17–24.

McPhaden, M. J., and A. E. Gill, 1987: Topographic scattering of equatorial kelvin waves. *J. Phys. Oceanogr.*, **17,** 82–96.

Sashegyi, K. D., and J. E. Geisler, 1987: A linear model study of cross-equatorial flow forced by summer monsoon heat sources. *J. Atmos. Sci.*, **44,** 1706–1722.

Schwerdtfeger, W. S., 1975: *Climates of Central and South America.* Vol. 12. Elsevier, 532 pp.

Silva Dias, P. L., and J. P. Bonatti, 1985: A preliminary study of the observed vertical mode structure of the summer circulation over tropical South America. *Tellus,* **37A,** 185–195.

——, —— and V. E. Kousky, 1987: Diurnally forced tropical circulation over South America. *Mon. Wea. Rev.*, **115,** 1465–1478.

——, W. H. Schubert and M. DeMaria, 1983: Large-scale response of the tropical atmosphere to transient convection. *J. Atmos. Sci.*, **40,** 2689–2707.

Virji, H., 1981: A preliminary study of summertime tropospheric circulation patterns over South America estimated from cloud winds. *Mon. Wea. Rev.*, **109,** 599–610.